Letter

Customized Vectorial Optical Fields in Homogeneous and Inhomogeneous Media

Yousuf Aborahama, Rajat K. Sinha, and Mo Mojahedi[*]

Edward S. Rogers Sr. Department of Electrical and Computer Engineering, University of Toronto, Toronto, Ontario, Canada M5S 3G4

The ability to design vectorial optical fields with desired properties in different media has a significant impact on many applications including microscopy, optical trapping, micromachining, and data communications. Here, we set up a framework, based on Maxwell's equations, that can be used to generate a desired three-dimensional vectorial optical field inside inhomogeneous and/or anisotropic media, where the generated field is either the exact or the closest physically possible rendition of the desired field. This approach is experimentally verified by generating two optical fields exhibiting interesting properties such as controllable states of polarization in a simple medium and self-healing behavior after a dielectric wall.

Introduction.—Structured light, in general, refers to the study and application of optical fields with customized properties (degrees of freedom) such as intensity profile [1,2], orbital angular momentum (OAM) [3,4], state of polarization (SOP) [5,6], and wavelength [7]. Whereas this field of study was initially concerned with controlling the intensity pattern at a particular plane, today, a wide range of tools exists to create customized field patterns in multiple planes using dynamic and geometric phase control. Spatial light modulators (SLMs) and metasurfaces [8,9] are two key technologies that have enabled the use of structured light in many applications. As SLM and metasurface technologies have been maturing, we find structured light at the core of many applications such as optical micromanipulations [10–12], imaging [13,14], optical communication systems [15,16], and remote sensing [17,18], to name a few.

While theoretical and experimental foundations of nondiffracting beams—a subclass of what is now referred to as the structured light—have been known for a while [19,20], the more intense interest in the field did not materialize till the more recent discovery of the self-accelerating beams [1]. Since then, researchers have invented alternative classes of beams that solve some of the existing limitations in the older ones. For example, nonparaxial Mathieu and Weber accelerating beams overcome the paraxial limitation of the Airy beams of Ref. [1], in addition to possessing more flexible trajectories such as circular or elliptical [21]. Engineering beams' trajectories is not limited to the aforementioned work, for example, researchers have demonstrated nonparaxial beams that follow helical

trajectories [22], accelerating light beams that follow convex trajectories [23], microscale caustic beams [24], and beams that change their direction of propagations "at will" [25]. Similarly, there has also been some work that takes the beam's polarization into account such as the accelerating and nondiffracting Helmholtz beams in Ref. [5], the nonparaxial accelerating beams that are solutions to Maxwell's equations in Ref. [26], and the so-called frozen waves that allow considerable control over the beam's polarization on axis [6]. Lastly, there have been efforts to engineer some parameters of the vortex beams, where researchers have generated beams that can change their local OAM with propagation [3], modify the local OAM abruptly [4], have the beam's center spot follow three-dimensional (3D) trajectories while maintaining the same topological charge [27], or a combination of both OAM and trajectory control [28]. However, it is worthwhile to point out that most of the aforementioned efforts were concerned with beams in simple media, and to the extent that some inhomogeneous media have been considered [29,30], they were only special cases with serious constraints on the SOP and the medium index of refraction.

Hence, in this letter, we introduce a general framework that can be used to design vectorial optical fields with predetermined polarization, amplitude, and phase distribution inside 3D inhomogeneous and anisotropic media, without the need to alter the media's optical properties. The generated optical field is guaranteed to be the closest possible rendition of the desired field, which also satisfies Maxwell's equations. The provided framework is experimentally verified by generating a beam that self-heals after scattering from a dielectric wall, after which a Bessel beam could not self-heal, and a beam that splits into two beams with orthogonal SOP in free space.

_____
[*]mojahedi@waves.utoronto.ca

Theoretical formulation.—Let $\mathcal{S} : \Omega \to \mathbb{C}^3$ represents the desired complex-valued vector field, defined inside some bounded open region $\Omega \subseteq \mathbb{R}^3$ with a piecewise smooth boundary $\partial\Omega$ that does not necessarily satisfy Maxwell's equations. On the other hand, let $\mathbf{E} : \Omega \to \mathbb{C}^3$ be a complex-valued vector field that satisfies Maxwell's equations, where our objective is to minimize the difference between $\mathbf{E}$ and $\mathcal{S}$ according to

$$\mathcal{E}[\mathbf{E}] = \int_\Omega \frac{1}{2}|\mathbf{E}(\mathbf{x}) - \mathcal{S}(\mathbf{x})|^2 d^3\mathbf{x}, \qquad (1)$$

subject to the constraint

$$\nabla \times (\boldsymbol{\mu}^{-1}(\mathbf{x})\nabla \times \mathbf{E}(\mathbf{x})) - \omega^2\boldsymbol{\epsilon}(\mathbf{x})\mathbf{E}(\mathbf{x}) = 0, \quad \forall\mathbf{x} \in \Omega, \tag{2}$$

where $\boldsymbol{\epsilon}(\mathbf{x})$ and $\boldsymbol{\mu}(\mathbf{x})$ are the complex permittivity and permeability tensors, respectively, chosen to be piecewise smooth. Note that we are going to assume that all the functions introduced in this work are sufficiently smooth, and from this point onward, we also drop the functions' arguments unless they are needed for clarification.

To account for the constraint in Eq. (2), we define an adjoint function $\boldsymbol{\Lambda} : \Omega \to \mathbb{C}^3$, and hence we obtain the Lagrangian functional

$$\mathcal{J}[\mathbf{E}] = \int_\Omega \frac{1}{2}|\mathbf{E} - \mathcal{S}|^2 + \mathrm{Re}[\boldsymbol{\Lambda} \cdot (\nabla \times (\boldsymbol{\mu}^{-1}\nabla \times \mathbf{E}) \\ - \omega^2\boldsymbol{\epsilon}\mathbf{E})]d^3\mathbf{x}. \tag{3}$$

Here, the inner product is defined for any $\mathbf{a}, \mathbf{b} \in \mathbb{C}^3$ in terms of their components as $\mathbf{a} \cdot \mathbf{b} = a_1^*b_1 + a_2^*b_2 + a_3^*b_3$. Next, we introduce the variation $\delta\mathbf{E}$ to $\mathbf{E}$ in Eq. (3) and expand the integrand to get

$$\mathcal{J}[\mathbf{E} + \delta\mathbf{E}]$$
$$= \int_\Omega \frac{1}{2}|\mathbf{E} - \mathcal{S}|^2 + \mathrm{Re}[(\mathbf{E} - \mathcal{S}) \cdot \delta\mathbf{E}]$$
$$+ \frac{1}{2}|\delta\mathbf{E}|^2 + \mathrm{Re}[\boldsymbol{\Lambda} \cdot (\nabla \times (\boldsymbol{\mu}^{-1}\nabla \times \mathbf{E}) - \omega^2\boldsymbol{\epsilon}\mathbf{E})]$$
$$+ \mathrm{Re}[\boldsymbol{\Lambda} \cdot (\nabla \times (\boldsymbol{\mu}^{-1}\nabla \times \delta\mathbf{E}) - \omega^2\boldsymbol{\epsilon}\delta\mathbf{E})]d^3\mathbf{x}. \tag{4}$$

Using F to denote the value assigned by the Lagrangian $\mathcal{J}$ to a given function $\mathbf{E}$, and keeping only the first-order terms in $\delta\mathbf{E}$ and $\delta\mathbf{E}^*$ along with using the fact that $\boldsymbol{\Lambda} \cdot \boldsymbol{\epsilon}\delta\mathbf{E} = \boldsymbol{\epsilon}^H\boldsymbol{\Lambda} \cdot \delta\mathbf{E}$, leads to the following first-order

variation of F with respect to $\mathbf{E}$ (denoted by δF)

$$\delta F = \int_\Omega \mathrm{Re}[(\mathbf{E} - \mathcal{S} - \omega^2\boldsymbol{\epsilon}^H\boldsymbol{\Lambda}) \cdot \delta\mathbf{E}]d^3\mathbf{x}$$
$$+ \int_\Omega \mathrm{Re}[\boldsymbol{\Lambda} \cdot (\nabla \times (\boldsymbol{\mu}^{-1}\nabla \times \delta\mathbf{E}))]d^3\mathbf{x}, \tag{5}$$

where $(\ )^H$ denotes the Hermitian. To proceed further, we use the relation $\mathbf{A} \cdot (\nabla \times \mathbf{B}) = (\nabla \times \mathbf{A}) \cdot \mathbf{B} - \nabla \cdot (\mathbf{A}^* \times \mathbf{B})$ (the conjugation appears due to the adopted definition of the inner product) and apply it twice along with the divergence theorem to arrive at

$$\delta F = \int_\Omega \mathrm{Re}[(\mathbf{E} - \mathcal{S} - \omega^2\boldsymbol{\epsilon}^H\boldsymbol{\Lambda}$$
$$+ \nabla \times ((\boldsymbol{\mu}^H)^{-1}\nabla \times \boldsymbol{\Lambda})) \cdot \delta\mathbf{E}]d^3\mathbf{x}$$
$$- \oint_{\partial\Omega} \mathrm{Re}[((\boldsymbol{\mu}^T)^{-1}\nabla \times \boldsymbol{\Lambda}^*) \times \delta\mathbf{E}$$
$$+ \boldsymbol{\Lambda}^* \times (\boldsymbol{\mu}^{-1}\nabla \times \delta\mathbf{E})] \cdot \mathbf{n}\, dS, \tag{6}$$

where $(\ )^T$ denotes the transpose, and $\mathbf{n}$ is the outward unit normal vector to the boundary. Using the fact that $(\mathbf{a} \times \mathbf{b}) \cdot \mathbf{c} = -(\mathbf{a} \times \mathbf{c}^*) \cdot \mathbf{b}^*$, we have

$$\delta F = \int_\Omega \mathrm{Re}[(\mathbf{E} - \mathcal{S} - \omega^2\boldsymbol{\epsilon}^H\boldsymbol{\Lambda}$$
$$+ \nabla \times ((\boldsymbol{\mu}^H)^{-1}\nabla \times \boldsymbol{\Lambda})) \cdot \delta\mathbf{E}]d^3\mathbf{x}$$
$$+ \oint_{\partial\Omega} \mathrm{Re}[((\boldsymbol{\mu}^H)^{-1}\nabla \times \boldsymbol{\Lambda}) \times \mathbf{n} \cdot \delta\mathbf{E}$$
$$+ \boldsymbol{\Lambda} \times \mathbf{n} \cdot (\boldsymbol{\mu}^{-1}\nabla \times \delta\mathbf{E})]\, dS. \tag{7}$$

This leads to the stationarity conditions

$$\nabla \times ((\boldsymbol{\mu}^H)^{-1}\nabla \times \boldsymbol{\Lambda}) - \omega^2\boldsymbol{\epsilon}^H\boldsymbol{\Lambda} + \mathbf{E} = \mathcal{S}, \quad \forall\mathbf{x} \in \Omega \tag{8a}$$

$$\boldsymbol{\Lambda} \times \mathbf{n} = 0, \ ((\boldsymbol{\mu}^H)^{-1}\nabla \times \boldsymbol{\Lambda}) \times \mathbf{n} = 0, \quad \forall\mathbf{x} \in \partial\Omega. \tag{8b}$$

At this point, it is worth noting that each integration in Eq. (7) can be expanded in terms of $\delta\mathbf{E}$ and $\delta\mathbf{E}^*$, which gives two equations for the stationarity conditions. Nonetheless, these two equations are complex conjugate of each other (recall that the functional is real), and when setting the variation to zero, it is necessary and sufficient to consider only one of them. Since all the boundary conditions (BCs) are in $\boldsymbol{\Lambda}$, we prefer to decouple the Eqs. (8a) and (2), which can be done by substituting the former in the later, leading

to

$$\nabla \times (\boldsymbol{\mu}^{-1} \nabla \times (\nabla \times ((\boldsymbol{\mu}^H)^{-1} \nabla \times \boldsymbol{\Lambda}))) - \omega^2 \boldsymbol{\epsilon} \nabla$$
$$\times ((\boldsymbol{\mu}^H)^{-1} \nabla \times \boldsymbol{\Lambda}) - \omega^2 \nabla \times (\boldsymbol{\mu}^{-1}(\nabla \times (\boldsymbol{\epsilon}^H \boldsymbol{\Lambda})))$$
$$+ \omega^4 \boldsymbol{\epsilon} \boldsymbol{\epsilon}^H \boldsymbol{\Lambda} = \nabla \times (\boldsymbol{\mu}^{-1} \nabla \times \boldsymbol{\mathcal{S}}) - \omega^2 \boldsymbol{\epsilon} \boldsymbol{\mathcal{S}}, \quad \forall \mathbf{x} \in \Omega,$$
$$\text{(9a)}$$

$$\boldsymbol{\Lambda} \times \mathbf{n} = 0, \quad ((\boldsymbol{\mu}^H)^{-1} \nabla \times \boldsymbol{\Lambda}) \times \mathbf{n} = 0, \quad \forall \mathbf{x} \in \partial\Omega.$$
$$\text{(9b)}$$

Once $\boldsymbol{\Lambda}$ is obtained, one can evaluate $\mathbf{E}$ using

$$\mathbf{E} = \boldsymbol{\mathcal{S}} - \nabla \times ((\boldsymbol{\mu}^H)^{-1} \nabla \times \boldsymbol{\Lambda}) + \omega^2 \boldsymbol{\epsilon}^H \boldsymbol{\Lambda}. \quad \text{(10)}$$

Undoubtedly, to evaluate Eq. (10), the solution of the boundary value problem (BVP) in Eq. (9) is needed; however, since at optical frequencies most materials are nonmagnetic, this motivates us to consider a more practical special case, where $\boldsymbol{\mu}/\mu_0$ is the identity matrix. Furthermore, for isotropic material, we can replace the permittivity tensor with a scalar permittivity ϵ. In this case, Eq. (9) can be simplified to

$$\nabla^{4\otimes} \boldsymbol{\Lambda} - k^2 \nabla^{2\otimes} \boldsymbol{\Lambda} - \nabla^{2\otimes}((k^*)^2 \boldsymbol{\Lambda})$$
$$+ |k|^4 \boldsymbol{\Lambda} = \nabla^{2\otimes} \mathcal{I} - k^2 \mathcal{I}, \quad \forall \mathbf{x} \in \Omega, \quad \text{(11a)}$$
$$\boldsymbol{\Lambda} \times \mathbf{n} = 0, \quad (\nabla \times \boldsymbol{\Lambda}) \times \mathbf{n} = 0, \quad \forall \mathbf{x} \in \partial\Omega, \quad \text{(11b)}$$

where $k^2 = \omega^2 \mu_0 \epsilon$, $\mathcal{I} = \mu_0 \boldsymbol{\mathcal{S}}$, and the operator $(\nabla^{n\otimes})$ is defined recursively as follows: $\nabla^{1\otimes} \boldsymbol{\Lambda} = \nabla \times \boldsymbol{\Lambda}$ and $\nabla^{n+1\otimes} \boldsymbol{\Lambda} = \nabla \times (\nabla^{n\otimes} \boldsymbol{\Lambda})$ for $n \geq 1$.

Results.—To design the optical fields presented in this letter, we choose the domain (Ω) to be a rectangular prism and place absorbers in front of all other boundaries, except for the boundary at the $z = 0$ plane. Next, for a desired vector field of interest ($\boldsymbol{\mathcal{S}}$), the BVP in Eq. (11) is solved using the finite-difference method. To do so, the equation and the BCs are discretized using second-order finite differences. The resulting system of linear equations is then solved via the biconjugate gradient stabilized method. Once the adjoint field $\boldsymbol{\Lambda}$ is found, $\mathbf{E}(x, y, 0)$ (i.e., the BC that is used to obtain the hologram) is calculated, which is used to generate the required hologram.

While the above formulation is valid for inhomogeneous and/or anisotropic media, the experimental examples, reported in this work, focus on the vectorial nature of the optical fields in homogeneous and inhomogeneous media. A schematic (top view) for the experimental setup is depicted in Fig. 1. In this setup, starting from the top left of Fig. 1, a 532-nm collimated Gaussian beam with vertical (along the y axis) linear polarization passes through a half-wave plate that is rotated at an angle of $22.5°$ (all angles
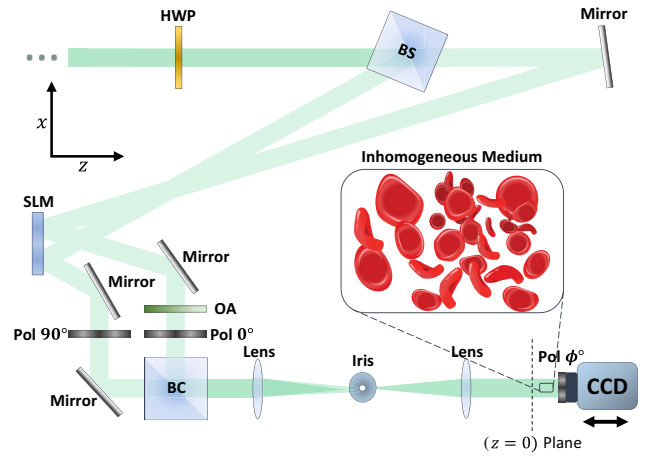

FIG. 1. Schematic of the experimental setup (top view). Two computer-generated holograms (one for each polarization) are displayed on a single reflective phase-only SLM, where each pattern is encoded on one half of the SLM to modulate two collimated 532-nm Gaussian beams with a diagonal (45°) linear polarization. The output patterns are then combined and filtered using a 4f system, which propagates in some inhomogeneous medium. The behavior of the optical field is then probed using a CCD camera (on a movable stage) equipped with a polarizer in order to analyze the polarization state of the optical field. Here, HWP is the half-wave plate, BS is the beam splitter, BC is the beam combiner, OA is the optical attenuator, and Pol refers to polarizers.

are with respect to the vertical axis) and then splits into two beams via a beam splitter. The first beam impinges on the right side of a reflective phase-only SLM with a pixel pitch of 8 μm, while the second beam is redirected through a mirror toward the left half of the same SLM. Displayed on each side of the SLM is a hologram that encodes the required BCs. The two modulated beams are then redirected toward polarizers oriented at 90° and 0°, with an additional attenuator in front of one of them, in order to ensure that both beams are at the same power level. The two beams are then combined via a beam combiner, resulting in a single beam. The resulting beam is then filtered and imaged using an iris, a 4f system, and a CCD camera on a moving stage, where additional polarizers (analyzers) are placed in front of the camera in order to determine the beam's SOP.

To demonstrate the ability of our approach to control and engineer the vectorial nature of the optical fields, we generate a beam that, after propagating a distance in air, will split into two orthogonal polarizations in a manner similar to using a polarization beam splitter. The beam's dynamics are depicted in Fig. 2. From Fig. 2(a), it is clear that at $z = 1.0$ cm, the beam contains components in both vertical (0°) and horizontal (90°) polarizations. However, once the beam splits (for example, at $z = 7$ cm), the left spot (spot A) is only vertically polarized while the right
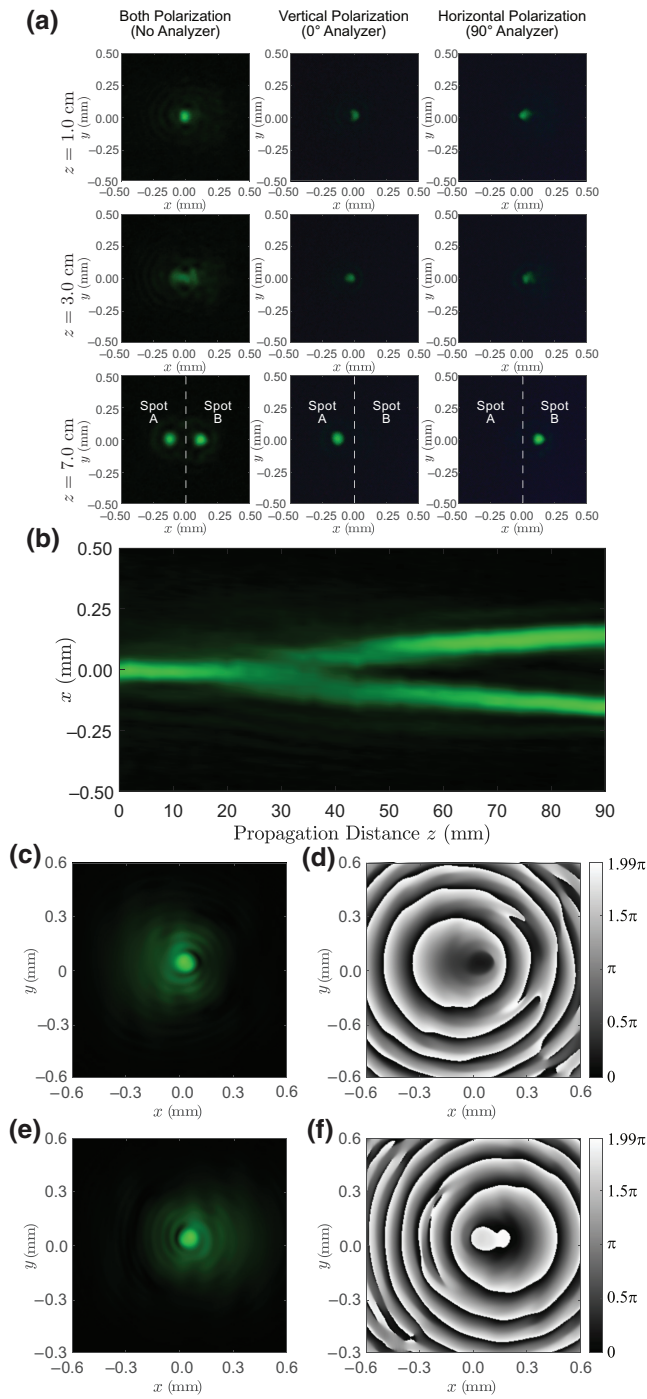
FIG. 2. Polarization beam-splitting pattern. (a) The transverse intensity profiles, where each row represents the measured field intensity at different propagation distances, while each column represents different analyzer angles, which shows the field SOP. These angles are for the vertical y axis. The beam initially contains two orthogonal polarizations, which splits, with propagation, into two beams with orthogonal SOPs. (b) The experimentally reconstructed longitudinal beam's intensity profile. (c)–(f) The magnitude (left) and phase (right) of the x component (top) and y component (bottom) of the electric field at the $z = 0$ plane, where black and white correspond to 0 and 1.99π phase shifts, respectively.

spot (spot B) is only horizontally polarized, mimicking the action of a polarization beam splitter. Figure 2(b) shows the beam intensity in the longitudinal plane (x-z plane), clearly demonstrating the intensity splitting in that plane. Figures 2(c) and 2(d) display the magnitude and phase associated with the x component of the field at the $z = 0$ plane (boundary plane), respectively, where the black and white colors associated with the phase figure corresponds to a relative phase of 0 and 1.99π. The same information for the y component of the field is presented in Figs. 2(e) and 2(f).
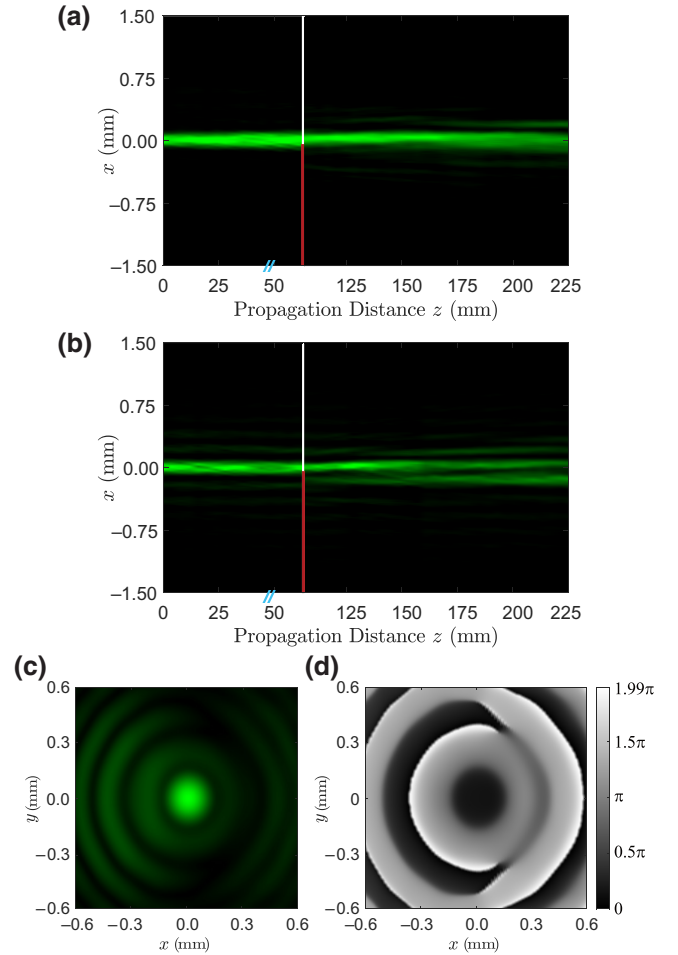
FIG. 3. Clearing a wall. (a) The experimentally reconstructed longitudinal intensity profile of the structured beam upon encountering a dielectric wall (in red) at $z = 63$ mm. The two blue slashes indicate a break in the z axis due to the difficulties associated with capturing that region using the CCD. (b) The experimentally reconstructed longitudinal intensity profile of a Bessel beam of approximately the same spot size as the structured beam facing the same walls. (c) The magnitude of the y component of the electric field (E_y) at the $z = 0$ plane. (d) The phase of E_y (on the right), where black and white correspond to 0 and 1.99π phase shifts, respectively.

We next turn our attention to generating a structured light in an inhomogeneous medium. For this example, we generate a beam that can clear a dielectric wall that cannot be cleared by common self-healing beams such as Bessel beams. The wall is made of a dielectric material with a thickness that introduces $135°$ phase shift. The behavior of the structured beam compared to the Bessel beam is shown in Fig. 3. Figure 3(a) shows the longitudinal intensity profile of the structured beam, where the red rectangle indicates the dielectric wall placed at $z = 63$ mm. Due to the presence of the wall, the intensity of the optical field in the vicinity of that region could not be captured. This is presented in the location of the break (in blue) along the z axis.

It is clear from this figure that the structured beam successfully clears the barrier while the Bessel beam [Fig. 3(b)] splits into two major beams after the dielectric barrier—accompanied with additional filamentation. It is worth pointing out that the Bessel beam is not able to self-heal because the dielectric wall has distorted the phase of all its rings, which makes the self-healing impossible. The magnitude of the field's y component at the boundary ($z = 0$ plane) is shown in Fig. 3(c). We note that the sidelobes on the right side of the figure are weaker than those on the left side, where the dielectric barrier is located. Figure 3(d) displays the phase of the y component of the field at the boundary ($z = 0$ plane). The figure also shows that the left and right sides of the second ring are out of phase, which explains why the structured beam (unlike the Bessel beam) can maintain its shape after the dielectric wall.

Conclusion.—In conclusion, we propose a framework based on analytical formulas that can be used to design an optical field with prechosen intensity, phase, and SOP in source-free inhomogeneous and/or anisotropic media. For cases where it is not physically possible to exactly generate the desired field in such media, the theoretical formulation guarantees that the generated field is the closest approximation to the desired field. The capabilities of the proposed analytical approach are experimentally demonstrated by generating two optical fields. The first example demonstrates our control over the vectorial nature of the beam by generating an optical beam that splits its polarization into two orthogonal states in air. In the second example, the structured beam traveling in an inhomogeneous medium is capable of passing a barrier, which the common self-healing beams such as Bessel beams cannot overcome. Finally, we expect the developed technique to have impacts on many applications such as optical micromanipulation, tweezers, imaging, and data communications, in addition to other wave-related phenomena.

[1] G. Siviloglou, J. Broky, A. Dogariu, and D. Christodoulides, Observation of Accelerating Airy Beams, Phys. Rev. Lett. **99**, 213901 (2007).

[2] A. H. Dorrah, M. Zamboni-Rached, and M. Mojahedi, Frozen waves following arbitrary spiral and snake-like trajectories in air, Appl. Phys. Lett. **110**, 051104 (2017).

[3] C. Schulze, F. S. Roux, A. Dudley, R. Rop, M. Duparré, and A. Forbes, Accelerated rotation with orbital angular momentum modes, Phys. Rev. A **91**, 043821 (2015).

[4] A. H. Dorrah, C. Rosales-Guzmán, A. Forbes, and M. Mojahedi, Evolution of orbital angular momentum in three-dimensional structured light, Phys. Rev. A **98**, 043846 (2018).

[5] P. Aleahmad, M.-A. Miri, M. S. Mills, I. Kaminer, M. Segev, and D. N. Christodoulides, Fully Vectorial Accelerating Diffraction-Free Helmholtz Beams, Phys. Rev. Lett. **109**, 203902 (2012).

[6] M. Corato-Zanarella, A. H. Dorrah, M. Zamboni-Rached, and M. Mojahedi, Arbitrary Control of Polarization and Intensity Profiles of Diffraction-Attenuation-Resistant Beams Along the Propagation Direction, Phys. Rev. Appl. **9**, 024013 (2018).

[7] A. H. Dorrah, M. Zamboni-Rached, and M. Mojahedi, Wavelength and topological charge management along the axis of propagation of multichromatic non-diffracting beams, JOSA B **36**, 1867 (2019).

[8] J. Wang and Y. Liang, Generation and detection of structured light: A review, Front. Phys. **9**, 263 (2021).

[9] J. Wang, Metasurfaces enabling structured light manipulation: Advances and perspectives, Chin. Opt. Lett. **16**, 050006 (2018).

[10] C. P. Jisha, A. Alberucci, J. Beeckman, and S. Nolte, Self-Trapping of Light using the Pancharatnam-Berry Phase, Phys. Rev. X **9**, 021051 (2019).

[11] V. Garcés-Chávez, D. McGloin, M. Padgett, W. Dultz, H. Schmitzer, and K. Dholakia, Observation of the Transfer of the Local Angular Momentum Density of a Multiringed Light Beam to an Optically Trapped Particle, Phys. Rev. Lett. **91**, 093602 (2003).

[12] A. O'neil, I. MacVicar, L. Allen, and M. Padgett, Intrinsic and Extrinsic Nature of the Orbital Angular Momentum of a Light Beam, Phys. Rev. Lett. **88**, 053601 (2002).

[13] Y. Xue, K. P. Berry, J. R. Boivin, C. J. Rowlands, Y. Takiguchi, E. Nedivi, and P. T. So, Scanless volumetric imaging by selective access multifocal multiphoton microscopy, Optica **6**, 76 (2019).

[14] S. Heist, C. Zhang, K. Reichwald, P. Kühmstedt, G. Notni, and A. Tünnermann, 5D hyperspectral imaging: Fast and accurate measurement of surface shape and spectral characteristics using structured light, Opt. Express **26**, 23366 (2018).

[15] A. E. Willner, H. Huang, Y. Yan, Y. Ren, N. Ahmed, G. Xie, C. Bao, L. Li, Y. Cao, Z. Zhao, *et al.*, Optical communications using orbital angular momentum beams, Adv. Opt. Photonics **7**, 66 (2015).

[16] G. Gibson, J. Courtial, M. J. Padgett, M. Vasnetsov, V. Pas'ko, S. M. Barnett, and S. Franke-Arnold, Free-space information transfer using light beams carrying orbital angular momentum, Opt. Express **12,** 5448 (2004).

[17] M. P. Lavery, F. C. Speirits, S. M. Barnett, and M. J. Padgett, Detection of a spinning object using light's orbital angular momentum, Science **341,** 537 (2013).

[18] N. Cvijetic, G. Milione, E. Ip, and T. Wang, Detecting lateral motion using light's orbital angular momentum, Sci. Rep. **5,** 15422 (2015).

[19] J. Stratton, *Electromagnetic Theory* (Mcgraw-Hill Book Company, Inc, New York, 1941).

[20] J. Durnin, J. Miceli, Jr., and J. H. Eberly, Diffraction-Free Beams, Phys. Rev. Lett. **58,** 1499 (1987).

[21] P. Zhang, Y. Hu, T. Li, D. Cannan, X. Yin, R. Morandotti, Z. Chen, and X. Zhang, Nonparaxial Mathieu and Weber Accelerating Beams, Phys. Rev. Lett. **109,** 193901 (2012).

[22] C. Vetter, T. Eichelkraut, M. Ornigotti, and A. Szameit, Generalized Radially Self-Accelerating Helicon Beams, Phys. Rev. Lett. **113,** 183901 (2014).

[23] E. Greenfield, M. Segev, W. Walasik, and O. Raz, Accelerating Light Beams along Arbitrary Convex Trajectories, Phys. Rev. Lett. **106,** 213902 (2011).

[24] L. Froehly, F. Courvoisier, A. Mathis, M. Jacquot, L. Furfaro, R. Giust, P. Lacourt, and J. Dudley, Arbitrary accelerating micron-scale caustic beams in two and three dimensions, Opt. Express **19,** 16455 (2011).

[25] Y. Aborahama, A. H. Dorrah, and M. Mojahedi, Designing the phase and amplitude of scalar optical fields in three dimensions, Opt. Express **28,** 24721 (2020).

[26] I. Kaminer, R. Bekenstein, J. Nemirovsky, and M. Segev, Nondiffracting Accelerating Wave Packets of Maxwell's Equations, Phys. Rev. Lett. **108,** 163901 (2012).

[27] J. Zhao, I. D. Chremmos, D. Song, D. N. Christodoulides, N. K. Efremidis, and Z. Chen, Curved singular beams for three-dimensional particle manipulation, Sci. Rep. **5,** 12086 (2015).

[28] Y. Aborahama and M. Mojahedi, Designing Optical Fields in Three Dimensions using Source-Boundary Transformations, Phys. Rev. Appl. **15,** 044019 (2021).

[29] Y. Aborahama and M. Mojahedi, Designing optical fields in inhomogeneous media, Opt. Lett. **46,** 5236 (2021).

[30] J. Quaglio and M. Zamboni-Rached, Transmission of spatial-shaped diffraction-resistant beams through stratified dielectric media: Finite energy formulation, JOSA A **35,** 2079 (2018).